Calcif Tissue Int (2012) 90:108–119
DOI 10.1007/s00223-011-9553-6

ORIGINAL RESEARCH

Longitudinal Assessment of In Vivo Bone Dynamics in a Mouse Tail Model of Postmenopausal Osteoporosis

Floor M. Lambers · Gisela Kuhn · Friederike A. Schulte · Kathleen Koch · Ralph Müller

Received: 11 July 2011 / Accepted: 17 November 2011 / Published online: 9 December 2011

Abstract Recently, it has been shown that transient bone biology can be observed in vivo using time-lapse micro-computed tomography (μCT) in the mouse tail bone. Nevertheless, in order for the mouse tail bone to be a model for human disease, the hallmarks of any disease must be mimicked. The aim of this study was to investigate whether postmenopausal osteoporosis could be modeled in caudal vertebrae of C57Bl/6 mice, considering static and dynamic bone morphometry as well as mechanical properties, and to describe temporal changes in bone remodeling rates. Twenty C57Bl/6 mice were ovariectomized (OVX, $n = 11$) or sham-operated (SHM, $n = 9$) and monitored with in vivo μCT on the day of surgery and every 2 weeks after, up to 12 weeks. There was a significant decrease in bone volume fraction for OVX (−35%) compared to SHM (+16%) in trabecular bone ($P < 0.001$). For OVX, high-turnover bone loss was observed, with the bone resorption rate exceeding the bone formation rate ($P < 0.001$). Furthermore there was a significant decrease in whole-bone stiffness for OVX (−16%) compared to SHM (+11%, $P < 0.001$). From these results we conclude that the mouse tail vertebra mimics postmenopausal bone loss with respect to these parameters and therefore might be a suitable model for postmenopausal osteoporosis. When evaluating temporal changes in remodeling rates, we found that OVX caused an immediate increase in bone resorption rate ($P < 0.001$) and a delayed increase in bone formation rate ($P < 0.001$). Monitoring transient bone biology is a promising method for future research.

Keywords Bone resorption · Osteoporosis · Ovariectomy · In vivo micro-computed tomography · High turnover

Osteoporosis, the most common bone disease, has become a major health problem worldwide [1]. Preclinical studies using animal models that approximate the progression of (postmenopausal) osteoporosis in humans are essential for the development of safer and more effective prevention and treatment of osteoporosis [2]. Removal of the ovaries (ovariectomy) in rats is a well-established model in postmenopausal osteoporosis research [3, 4]. Ovariectomy leads to estrogen depletion, which in turn causes bone loss. With this technique, osteoporosis-related bone loss has often been investigated in the proximal tibia of rats [5–7]. A smaller effect of ovariectomy-induced bone loss has been seen in the distal tibia [8, 9] and lumbar vertebra [10], while no bone loss has been observed in caudal (tail) vertebrae of rats [11, 12].

In the past decade ovariectomy of mice has emerged as a model for osteoporosis because mouse models have several advantages over rat models. The accessibility of the mouse genome facilitates gene identification and deletion for the study of modifying molecular mechanisms of osteoporosis [13]. Also, the costs are lower due to cheaper housing of mice and smaller amounts of drugs that are needed for mice. Furthermore, there are many mouse strains to choose from which can represent a specific phenotype (e.g., low–bone mass C57Bl/6 mice or high-bone mass C3H mice). In mice the most frequently investigated site is the distal femur, where large amounts of bone loss occur after ovariectomy [14, 15]. At other sites there are some

The authors have stated that they have no conflict of interest.

F. M. Lambers · G. Kuhn · F. A. Schulte · K. Koch · R. Müller (✉)
Institute for Biomechanics, ETH Zürich,
Wolfgang-Pauli-Strasse 10, 8093 Zürich, Switzerland
e-mail: ram@ethz.ch

conflicting results. Nevertheless, in mice ovariectomy-induced bone loss is strain- and skeletal site-dependent [16–19].

Recently, it has been shown that transient bone biology can be observed in vivo using time-lapse micro-computed tomography (μCT) in the mouse tail bone. Nevertheless, in order for the mouse tail bone to be a model for human disease, the hallmarks of any disease must be mimicked. To our knowledge, ovariectomy-induced bone loss has not been investigated in caudal vertebrae of mice. However, it would be very convenient if, instead of the distal femur, a caudal vertebra could be used as an osteoporosis model because this would have several advantages: (1) it is more easily accessible for high-resolution imaging, (2) the whole bone can be imaged within an acceptable scan time and dose, (3) both cortical and trabecular bone can be imaged, (4) the amount of trabecular bone is relatively high in vertebrae, and (5) it is accessible for mechanical loading [20, 21].

In order to have a valid postmenopausal osteoporosis model, several main requirements have to be fulfilled [2, 3]. First, there should be a large amount of bone loss as women can lose up to 20% of their bone mass in the first 5–7 years that follow menopause [22]. Second, the model should demonstrate high-turnover bone loss as typically postmenopausal bone deterioration progresses by an increased bone formation rate and an increased bone resorption rate, with bone resorption exceeding bone formation [23]. Third, as a result of the bone loss, fragility fractures should be present in the bone. Fragility fractures are uncommon in rodents [24], but the strength of the bone must decrease. Therefore, it has been established that bone strength or stiffness can be assessed with mechanical testing [25, 26] or finite element analysis [27] as a surrogate for bone fragility.

We hypothesized that ovariectomy would induce bone loss in the caudal vertebrae of C57Bl/6 J mice since these vertebrae increase bone mass upon cyclic loading [20] and, thus, seemed responsive to interventions. Furthermore, when osteoporosis-related bone loss was evaluated in caudal vertebrae of SAMP6 mice, a senescence-accelerated mouse strain, the bone mass at 4 and 12 months of age was significantly lower than in controls [28]. To investigate whether the above-mentioned requirements were achieved for caudal vertebrae of C57Bl/6 J mice, several methods were used. First, to monitor the extent of bone loss and changes in the bone microstructure after ovariectomy, the sixth caudal vertebra was scanned with in vivo μCT at multiple time points. Second, to investigate the presence of high-turnover bone loss, bone dynamic morphometric parameters were calculated with a recently validated in vivo technique [29]. This technique allows the quantification of dynamic bone formation and resorption parameters in 3D over time from serial μCT scans. Third, to investigate changes in stiffness of the bones, micro-finite element (μFE) analysis was performed.

Previous reports have described temporal patterns in bone microstructure or mineralization as an effect of ovariectomy in rats or mice. Nevertheless, to better understand how ovariectomy influences osteoblast and osteoclast activity, the transient patterns of bone remodeling rates should be described as well. Little attention has been given to this as until recently it was challenging to determine how bone remodeling rates change over time using histomorphometry (loss of label) or biochemical markers (not site-specific). The recently validated in vivo technique to extract dynamic bone morphometric parameters from serial in vivo μCT scans [29], on the other hand, allows us to investigate temporal changes in remodeling rates, giving an accurate indication of how formation and resorption sites are modulated by ovariectomy. This information is essential for gaining a better understanding of ovariectomy-induced bone loss.

In summary, the aim of this study was to investigate whether caudal vertebrae of C57Bl/6 J mice are a valid model for postmenopausal osteoporosis, taking into account the bone microstructure, dynamic morphometric parameters, and mechanical properties. A further objective was to provide a more detailed description of temporal patterns in dynamic bone remodeling rates induced by ovariectomy.

Methods

Animals

Twenty 14-week-old female C57Bl/6 J mice (RCC, Füllinsdorf, Switzerland) were housed in an environmentally controlled room in a 12-h light/dark cycle, with free access to standard diet and tap water. After 1 week of settling, mice were ovariectomized bilaterally (OVX, $n = 11$) or sham-operated (SHM, $n = 9$). The analgesic buprenorphin (Temgesic, 0.1 mg/kg) was injected twice daily on the day of surgery and for the following 2 days, to avoid pain. Mice were monitored closely and weighed three or four times per week in the first 2 weeks postoperation and before each μCT scan thereafter. Mice were chosen to be 3 months because it was shown previously that there is a rapid increase in bone volume fraction up to 12 weeks, which deviates <1.1% afterward up to 32 weeks in the third lumbar vertebra in C57Bl/6 mice [30]. All procedures were performed under isoflurane anesthesia (2–2.5%, 0.4 l/min) delivered through a nose mask. All experimental procedures were approved by the local laboratory animal care and use committee (Kantonales Veterinäramt Zürich, Zürich, Switzerland).

In Vivo μCT

Descriptions and nomenclature in the following sections are in line with a recent review on guidelines for the assessment of bone microstructure with μCT [31]. The sixth caudal vertebra (CV6) was scanned with in vivo μCT (vivaCT 40; Scanco Medical, Brüttisellen, Switzerland), on the day of surgery and consecutively every 2 weeks for 12 weeks, resulting in a total of seven images per mouse. Mice were scanned under isoflurane anesthesia in a holder heated at just below body temperature (35°C). Vitamin A cream was applied to the eyes to prevent desiccation. The region of interest was selected by counting the vertebrae from the first caudal vertebra (at the sacrum) in a dorsoventrally taken scoutview. CV6 was measured completely in two connecting stacks, comprising a length of 4.4 mm. The scanner was operated at 55 kVp and 145 μA, with an integration time of 200 ms and no frame averaging. We captured 1,000 projections per 180°, leading to a nominal isotropic resolution of 10.5 μm. A beam hardening correction algorithm provided by Scanco Medical was applied to all scans. The estimated dose rate was 32 mGy/min over a period of 20 min. The CT scanner was calibrated weekly for mineral equivalent value and monthly for determining in-plane spatial resolution. All raw μCT data were reconstructed with the dorsal side of the vertebra facing upward. For the basal scan, the long axis of the bone was aligned with the z-axis, to facilitate the conversion of the μCT data into μFE models. Follow-up scans were translated and rotated to match the previous measurement using rigid registration. A 3D constrained gaussian filter (sigma 1.2, support 1) was applied, after which images were segmented by a fixed thresholding procedure (22% of maximum gray-scale value).

Static Bone Morphometry

Trabecular and cortical regions were selected from the thresholded images by automated masks. For the trabecular mask, growth plates were eliminated (top and bottom 10%) and the space almost void of trabecular bone (the middle 26%) was excluded from the analysis. Within the regions of interest, bone structural parameters were calculated with a direct 3D model-independent algorithm, including bone volume fraction (BV/TV), trabecular thickness (Tb.Th), and trabecular number (Tb.N).

For the calculation of cortical bone morphometric indices, the trabecular structure was removed and 12.5% from the top and bottom was eliminated to exclude the regions close to the growth plates. The morphological indices in the cortical region included total volume (Ct.TV), marrow volume (Ct.MV), cortical area fraction (Ct.Ar/Tt.Ar), and average cortical thickness (Ct.Th). Ct.Ar/Tt.Ar was calculated by dividing the cortical bone volume (Ct.BV) by Ct.TV, which was possible because the length of scanned volumes—Ct.BV and Ct.TV—were the same (i.e. Ct.Ar/Tt.Ar = (Ct.BV/number of slices)/(Ct.TV/number of slices)). All bone structural parameters were normalized to the first time point for each mouse to calculate percentage changes.

Dynamic Bone Morphometry

A method to visualize sites of bone formation and bone resorption from serial in vivo μCT data was developed previously [7]. This method was extended to enable the calculation of dynamic bone morphometric parameters in the trabecular region, as recently validated [29]. For this procedure, scans of follow-up time points were rotated and translated (registered) to match the orientation of the previous scan by applying a rigid registration algorithm proposed by Thevenaz et al. [32]. This registration algorithm consists of a pyramid approach where in each step the mean square difference of intensities between a reference (first time point) and a template (following time point) data set is minimized. Thus, the same cross section (or bone volume) can be visualized at serial time points, which allows observation of the changing bone microstructure over time (see Fig. 1a). From these images it is then possible to visually observe where bone was formed or resorbed between time points, but to better localize these sites of formation and resorption and to allow morphometric analysis of remodeling sites, follow-up scans were superimposed on each other. With this step, sites present only at the initial time point, sites present only at the subsequent time point, and sites present at both time points can be colored differently (see Fig. 1b). The voxels present only at the initial time point must have been removed between scans and are considered resorbed bone (blue). Similarly, voxels present only at the subsequent time point must have been added and therefore are representative of formed bone (yellow). Furthermore, for voxels present at both time points no measureable changes occurred, and these sites are regarded as constant bone (gray). To explain this technique in comparison to dynamic histomorphometry, the complete surface of the bone at the initial time point can be considered as the first label, while the complete surface of the following time point can be considered as the second label. The volume between these bone surface labels can then be considered resorbed or formed bone. When the second label resides within the bone of the initial time point, bone resorption has occurred, while when the second label is where the bone marrow would have been at the initial time point, bone was formed

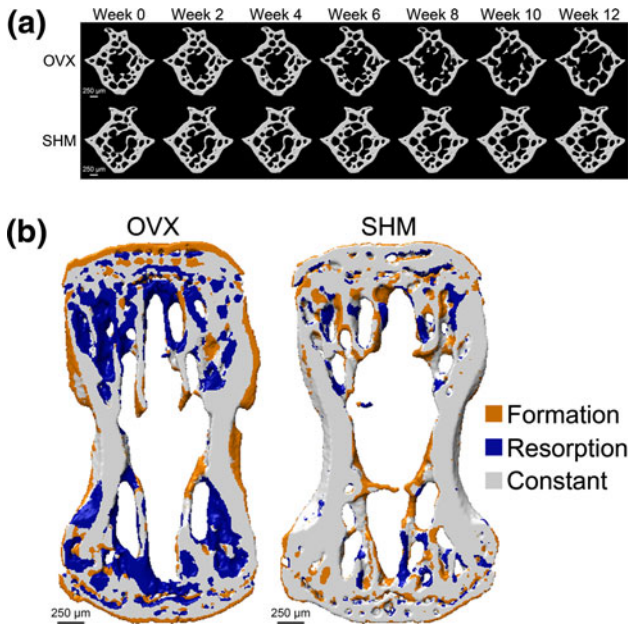

Fig. 1 Visualization of bone loss. **a** Bone microstructure (cross-section) of representative vertebrae of the OVX and SHM groups for all time points at which in vivo µCT scans were performed. **b** Images of overlaid bone microstructure (cross section) of weeks 0 and 12 of representative vertebrae of the OVX and SHM groups. Structures in *yellow* denote bone was formed between weeks 0 and 12 (only present at week 12). Structures in *blue* indicate bone was resorbed between weeks 0 and 12 (only present at week 0). *Gray* structures were present at both time points

between scans. The difference of our approach compared to histomorphometry is that labels cannot be lost, labels are also existent for resorbed sites, and parameters describing the volume, thickness, and surface of remodeling sites are calculated directly in 3D.

In our approach, for each mouse, registered binary µCT images acquired at consecutive time points were overlaid to calculate bone formation and bone resorption for each interval (i.e., week 0–2, week 2–4, week 4–6, week 6–8, week 8–10, and week 10–12). Similar to histomorphometry, rates calculated over a time interval were considered the value at the later time point (i.e., the value at week 2 is calculated from the overlay of week 0–2). With this procedure, volumes of bone formation or resorption could be identified and analyzed morphometrically. These parameters were defined in analogy to histomorphometric indices and included bone formation rate (BFR), bone resorption rate (BRR), mineral apposition rate (MAR), mineral resorption rate (MRR), mineralizing surface (MS), eroded surface (ES), the number of formation sites per bone volume (NFS), and the number of resorption sites per bone volume (NRS). A full description of the procedure to calculate the dynamic morphometric properties has been presented and validated [29].

Finite Element Analysis

For each mouse at each time point, segmented image data were converted into 3D linear elastic µFE models, where the disc volumes were replaced by bone to facilitate uniform loading of the end plates. The discs were created by setting a seeding point at the neutral axis (where the bending moment is zero) at both the proximal and distal ends, forming a circle with a set radius from the seeding points and filling all voxels between this circle and the bone. All voxels were converted to eight-node brick elements, rendering models of approximately 1.8 million elements. For both the bone and the disc a Young's modulus of 14.8 GPa and a Poisson ratio of 0.3 were assigned to each element, as previously validated for caudal vertebrae [33]. The top was displaced 0.1%, while the bottom was constrained in all directions. The models were solved using a parallel finite element package (ParFE) with an algebraic multigrid preconditioner. The simulations ran on a Cray XT5 supercomputing system composed of 22,128 CPU cores and 29 TB of RAM at the Swiss National Supercomputing Center (CSCS, Manno, Switzerland).

The resulting force was calculated and used to scale the output parameters to the same force (4 N). The real force that CV6 is subjected to under physiological conditions is unknown, but it has recently been found using a novel bone loading estimation method that external loading conditions of CV6 are in the range of 4 N [34]. Changes in the stiffness of the whole bone were analyzed from the µFE results.

The change in strain energy density (SED) was calculated in trabecular and cortical bone in three regions: the proximal region, the middle region, and the distal region (see Fig. 5). In each of these regions the fraction of load carried by the cortical bone was calculated by determining the strain energy stored in the cortex as a fraction of the total strain energy [35]. To quantify changes in mechanical properties over time, the data were normalized to the first time point for each mouse.

Statistical Analysis

Statistical analysis was performed with the software package R (www.r-project.org/). A Kolmogorov-Smirnov test verified that the data were normally distributed. Repeated-measurements ANOVA, implemented as a linear mixed-effects model, was performed to detect significant differences in bone parameters between groups and over time. With this test, significant differences were determined for effect of time, effect of group, and the interaction between time and group, which indicated whether the time course developed differently between groups. Furthermore, to identify at which time points OVX and SHM

were significantly different, Student's *t*-tests were performed at each time point with Bonferroni post hoc corrections for multiple comparisons. $P < 0.05$ was considered significant. All data are shown as mean ± standard error.

Results

Animals

All animals remained healthy and gained weight throughout the experiment. There was a trend that OVX mice gained more weight than SHM mice. Four mice were excluded because the wrong vertebra was scanned at one of the time points (two SHM, two OVX).

Static Bone Morphometry

As can visually be seen in Fig. 1a, for OVX the bone microstructure deteriorated over time, while for SHM the bone microstructure remained relatively constant. The change in BV/TV over time was significantly different between groups ($P < 0.001$); it increased 16% for SHM ($P < 0.001$ over time) and decreased 35% for OVX ($P < 0.001$ over time) compared to baseline (Fig. 2a). Both groups showed a similar increase in BV/TV in the first 2 weeks, after which there was a clear difference between groups. The decrease in BV/TV for OVX was mainly caused by thinning and perforation of trabeculae, leading to a somewhat delayed decrease in the number of trabeculae. Tb.Th decreased 12% for OVX ($P < 0.001$ over time), which was significantly different from SHM ($P < 0.001$), where Tb.Th increased 6% ($P < 0.001$ over time, Fig. 2b). Tb.N started to decrease roughly 2 weeks later, resulting in an 11% decrease for OVX at 12 weeks ($P < 0.001$ over time), which was significantly different ($P < 0.001$) from SHM, where Tb.N remained constant (Fig. 2c). The absolute values of these parameters are shown in Table 1.

In the cortex, a similar progression of bone loss was observed: Ct.Ar/Tt.Ar developed significantly different over time between groups ($P < 0.001$); for SHM, Ct.Ar/Tt.Ar increased 3% ($P < 0.001$ over time), while for OVX it decreased 9% ($P < 0.001$ over time, Fig. 2d). This came with a concomitant decrease in Ct.Th of 5% for OVX ($P < 0.001$ over time), while for SHM this increased by 3% ($P < 0.001$ over time and $P < 0.001$ between groups,

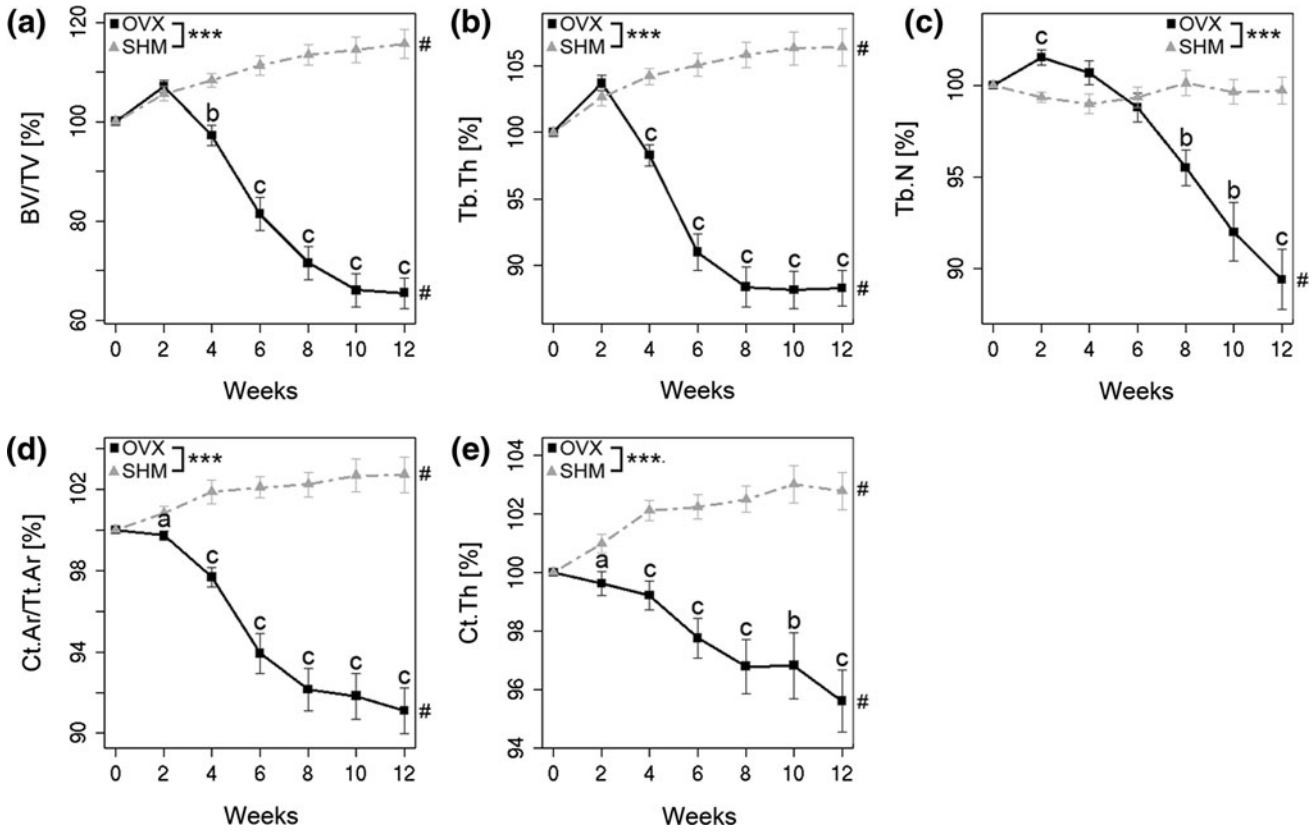

Fig. 2 Static bone morphometric parameters over time. **a** Trabecular bone volume fraction (BV/TV), **b** trabecular thickness (Tb.Th), **c** trabecular number (Tb.N), **d** cortical area fraction (Ct.Ar/Tt.Ar), **e** cortical thickness (Ct.Th). ***$P < 0.001$ between groups and $^{\#}P < 0.001$ over time as tested with repeated-measurements ANOVA. $^{a}P < 0.05$, $^{b}P < 0.01$, and $^{c}P < 0.001$ between groups as tested with Student's *t*-test with Bonferroni post hoc correction

Table 1 Bone structural parameters in trabecular and cortical bone at first and last time points for both groups

	Week 0	Week 12	*P*
Trabecular			
BV/TV (%)			
OVX	22.1 ± 2.4	14.4 ± 1.7	<0.001
SHM	19.9 ± 3.6	22.8 ± 3.1	
Tb.Th (μm)			
OVX	79.0 ± 0.0	70.0 ± 0.0	<0.001
SHM	76.0 ± 0.0	80.0 ± 10.0	
Tb.N (1/mm)			
OVX	3.21 ± 0.19	2.87 ± 0.23	<0.001
SHM	3.15 ± 0.25	3.14 ± 0.22	
Cortical			
Ct.TV (mm^3)			
OVX	5.22 ± 0.38	5.60 ± 0.37	<0.001
SHM	5.44 ± 0.39	5.55 ± 0.41	
Ct.MV (mm^3)			
OVX	2.92 ± 0.26	3.35 ± 0.30	<0.001
SHM	3.21 ± 0.42	3.23 ± 0.43	
Ct.Ar/Tt.Ar (%)			
OVX	44.2 ± 1.8	40.2 ± 2.1	<0.001
SHM	41.0 ± 4.7	42.1 ± 4.4	
Ct.th (μm)			
OVX	161 ± 10	154 ± 10	<0.001
SHM	152 ± 10	156 ± 10	

P values denote significant differences between groups as tested with repeated-measurements ANOVA

BV/TV bone volume fraction, *Tb.Th* trabecular thickness, *Tb.N* trabecular number, *Ct.TV* total volume of cortical mask, *Ct.MV* marrow volume, *Ct.Ar/Tt.Ar* cortical area fraction, *Ct.Th* average cortical thickness

Fig. 2e). The cortex was reduced mostly on the endosteal side, while some apposition was present at the periosteal side. This was also confirmed by a significantly greater increase of 15% in Ct.MV for OVX ($P < 0.001$ over time) compared to no change for SHM ($P < 0.001$ between groups) and a significantly greater increase of 7% in Ct.TV for OVX ($P < 0.001$ over time) compared to a 2% increase for SHM ($P < 0.001$ over time and $P < 0.001$ between groups, Table 1).

Dynamic Bone Morphometry

BFR was elevated for OVX compared to SHM starting from 8 weeks (Fig. 3a), while BRR was greater for OVX than for SHM over the whole time range (Fig. 3b). On average BFR was 1.6 times greater for OVX than SHM ($P < 0.05$) and BRR was 3.7 times greater for OVX than SHM ($P < 0.001$). This is also visually evident in Fig. 1b, where for OVX there are more yellow structures (indicating BFR) and many more blue structures (indicating BRR) than for SHM. MAR, which represents the thickness of formation sites, was significantly greater for OVX than SHM ($P < 0.01$, Fig. 3c). Also, MRR, which represents the depth of resorption sites, was significantly greater for OVX than SHM ($P < 0.001$, Fig. 3d). On average MAR was 1.2 times greater and MRR 1.7 times greater for OVX than SHM. MS, which represents the surface of formation sites, was significantly smaller for OVX than SHM ($P < 0.001$, Fig. 3e). ES, which represents the surface of resorption sites, was significantly greater for OVX than SHM ($P < 0.001$, Fig. 3f). For OVX the profiles of MS and ES had the opposite shape: when MS seemed the smallest at week 6 (on average 1.5 times smaller than for SHM), ES seemed the largest (on average 1.4 times larger than for SHM).

To investigate whether the profiles for ES and MS were an effect of changes in the amount of sites or an effect of changes in the shape of formation and resorption sites, the numbers of formation and resorption sites per bone volume were calculated. NFS was significantly smaller for OVX than for SHM ($P < 0.001$, Fig. 3g), and NRS was significantly smaller for OVX than for SHM ($P < 0.001$, Fig. 3h). No changes were seen for NFS and NRS over time, indicating that when MS decreased this was mostly because the surface of formation sites decreased, rather than because the number of formation sites decreased. Similarly, a change in ES was mainly caused by a change in the surface of resorption sites.

This gives evidence that both the shape and the number of formation and resorption sites were modulated by OVX. Formation sites were smaller in number, with a smaller surface but an increased thickness. At the same time the quantity of resorption sites was less, with sites showing a broader surface and greater thickness and becoming more massive. Even though the number of formation and resorption sites was smaller for OVX than SHM, the thicknesses were so much increased and the surface increased to such an extent for resorption sites that the volumes of formation and resorption were larger for OVX than for SHM.

When the ratios between formation and resorption were explored, it could be seen that BFR was greater than BRR for SHM, while BRR was greater than BFR for OVX. The ratio was significantly smaller for OVX than for SHM ($P < 0.001$). Similarly, the ratio between MS and ES was significantly smaller for OVX than for SHM ($P < 0.001$), and the ratio between MAR and MRR was significantly smaller for OVX than for SHM ($P < 0.001$); on the contrary, the ratio between NFS and NRS was significantly greater for OVX than for SHM ($P < 0.001$). On average MRR was greater than MAR for OVX and ES was greater than MS for OVX, while NRS was smaller than NFS for

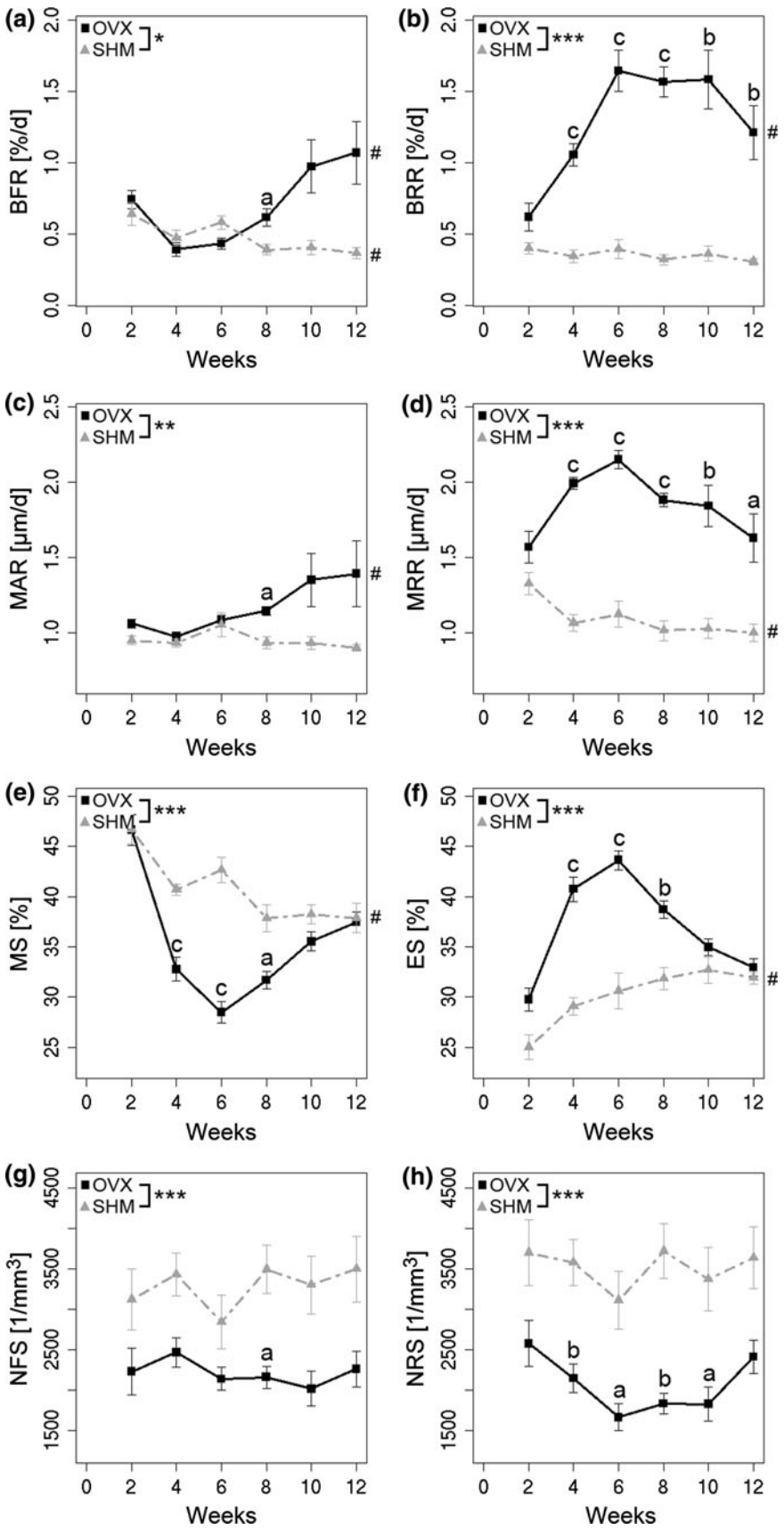

Fig. 3 Dynamic bone morphometry over time. **a** Bone formation rate (BFR), **b** bone resorption rate (BRR), **c** mineral apposition rate (MAR), **d** mineral resorption rate (MRR), **e** mineralizing surface (MS), **f** eroded surface (ES), **g** number of formation sites per bone volume (NFS), **h** number of resorption sites per bone volume (NRS). The *x*-axis indicates the time points from which the dynamic parameters were determined; e.g., week 2 indicates from an overlay of week 2 on week 0. $^{*}P < 0.05$, $^{**}P < 0.01$, $^{***}P < 0.001$ between groups and $^{\#}P < 0.01$ over time as tested with repeated-measurements ANOVA. $^{a}P < 0.05$, $^{b}P < 0.01$, and $^{c}P < 0.001$ between groups as tested with Student's *t*-test with Bonferroni post hoc correction

OVX. This indicates that for OVX the sites of resorption were less numerous but more massive or that multiple sites had merged into fewer but larger sites.

Finite Element Analysis

From μFE analysis it was found that the stiffness of CV6 reduced 16% for OVX ($P < 0.001$ over time), which was significantly different from SHM ($P < 0.001$), where the stiffness increased 11% ($P < 0.001$ over time, Fig. 4a). SED increased significantly in the proximal and distal regions of both cortical and trabecular bone for OVX, while decreases were observed for SHM in the proximal region, with significant differences between OVX and SHM (Table 2). The increase in SED for OVX in both trabecular and cortical regions was also visually apparent (Fig. 4b). In the middle region, no significant differences were found between OVX and SHM. The fraction of load carried by the trabecular bone (Fig. 5) was much smaller than the load carried by the cortical bone in all of the regions, especially the middle region. With the decrease in bone volume fraction for OVX, significantly less load was carried by the trabecular bone in the distal region ($P < 0.01$ over time) and proximal region ($P < 0.001$ over time). On the contrary, for SHM the fraction of load carried by the trabecular bone increased significantly over time in all three regions ($P < 0.001$ over time).

Discussion

In this study we showed that the sixth caudal vertebra of C57Bl/6 J mice is a valid model for studying osteoporosis-related bone loss, by showing that ovariectomy led to high-turnover bone loss, with a subsequent reduction in bone stiffness. Consequently, it is proposed that the caudal vertebrae of ovariectomized mice can be used as an alternative model to study postmenopausal osteoporosis.

Table 2 Percentage change in SED after 12 weeks in trabecular and cortical bone in the three subregions

	Trabecular		Cortical	
	OVX	SHM	OVX	SHM
Distal	+37%	NS*	+29%	NS**
Middle	NS	NS	NS	−7%
Proximal	+50%	−10%**	+34%	−11%**

NS no significant change over time

*$P < 0.01$ and **$P < 0.001$ between OVX and SHM as tested with repeated-measurements ANOVA

With regard to bone structural parameters, we confirmed that ovariectomy caused a significant decrease in BV/TV and a significant decrease in Ct.Ar/Tt.Ar, with a greater bone loss in the trabecular than cortical region, as has been reported in previous studies at other skeletal sites in mice [16, 19, 36, 37]. The greater loss in the trabecular bone can be explained by the fact that the cortical bone is more important for mechanical stability of the bone, while the trabecular bone, as it has a larger surface, is more important for homeostasis [38]. This observation was also confirmed by the fact that, in the sixth caudal vertebra, cortical bone carried relatively more load and that this fraction became even larger after ovariectomy.

The trabecular bone volume fraction showed a delayed decrease, starting only 2 weeks postovariectomy, which was unexpected as such a delay has not been shown previously by others for other bones. In a study with time-lapse images of the tibia in C57Bl/6 J mice up to 5 weeks after surgery, no significant effect of OVX was found [19]. In cross-sectional studies, several others found significant decreases in BV/TV 2 weeks after OVX in the tibia in C3H/Hen mice [37] and 4 weeks after ovariectomy in lumbar vertebrae, proximal tibia, and distal femur in C57Bl/6 J mice [16, 18]. Additionally, in rats, where time-lapse images of the proximal tibia were available, an initial delay in the decrease has not been described [5, 6].

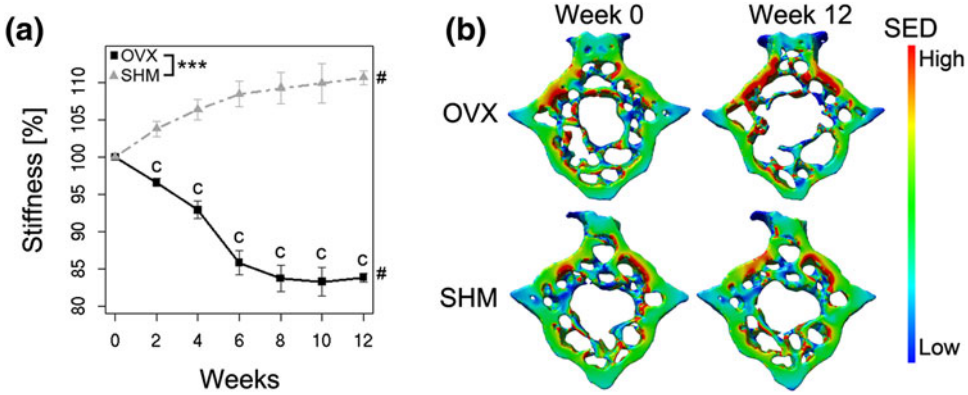

Fig. 4 **a** Stiffness of the whole bone over time. ***$P < 0.001$ between groups and $^{\#}P < 0.001$ over time as tested with repeated-measurements ANOVA. $^{c}P < 0.001$ between groups as tested with Student's *t*-test with Bonferroni post hoc correction. **b** Visualization of SED in cross sections of representative mice at first and last time points. *Red* denotes high SED, while *blue* represents low SED (*see scale bar*)

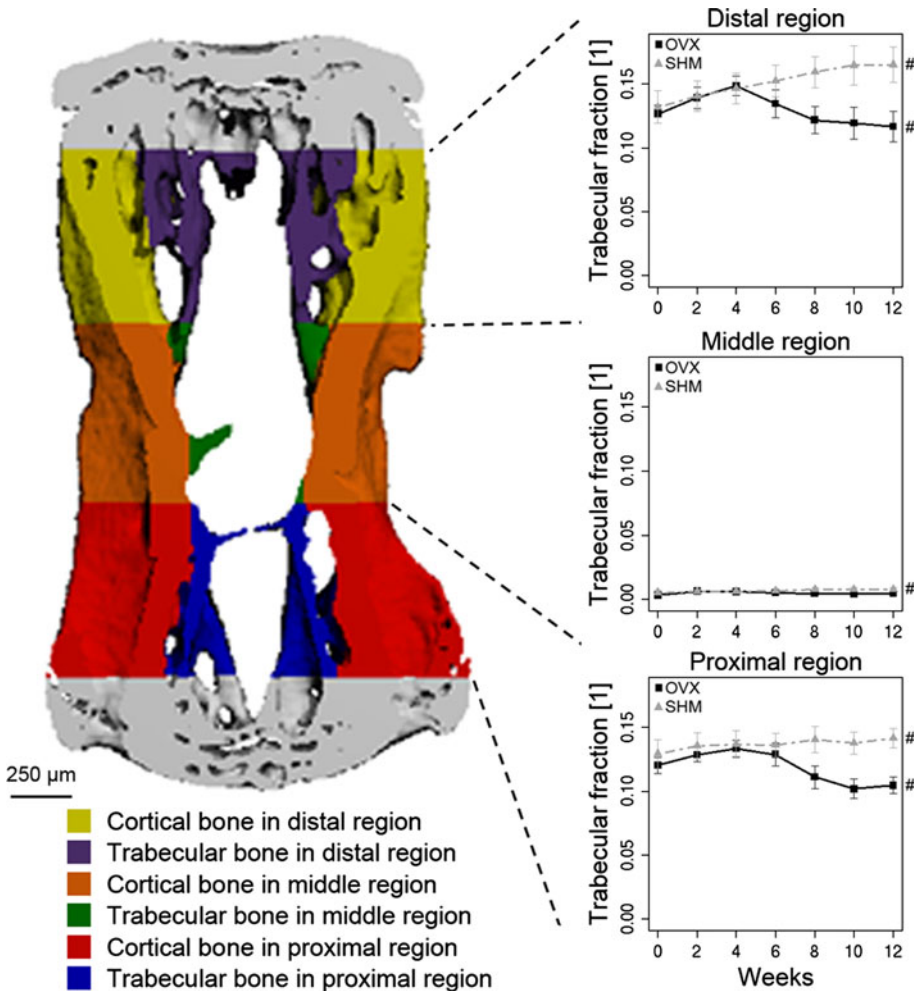

Fig. 5 Fraction of load carried by trabecular bone in the distal region (*upper*), middle region (*middle*), and proximal region (*lower*). The selection of the regions is shown in the colored image on the left. $^{\#}P < 0.001$ over time as tested with repeated-measurements ANOVA

A finding that coincides with the initial lack of response to ovariectomy is that in rats skeletal sites with fatty (yellow) bone marrow content react slower to ovariectomy than sites with hematopoietic (red) bone marrow [10]. It has also been shown that in rats the fifth caudal vertebra consists of fatty bone marrow [12]. Thus, it might be that in mice the sixth caudal vertebra contains fatty (yellow) bone marrow and that this influences the response to ovariectomy, leading to delayed bone loss. Oftentimes the presence of yellow marrow in the tail of the mouse has been regarded as a negative effect. Nevertheless, in elderly osteoporotic subjects, bone marrow is also predominantly yellow [39]. Furthermore hematopoietic stem cells and progenitor cells of the red bone marrow are highly sensitive to the effects of ionizing radiation. On the other hand, yellow bone marrow, where most cells are fat cells, is less sensitive to radiation effects [40]. Therefore, the presence of yellow bone marrow may also be seen as an advantage over other models of postmenopausal bone loss.

BV/TV increased throughout the study for SHM mice. This is in agreement with a previous study where an increase in BV/TV up to 20 months of age was reported in the seventh caudal vertebra in BALB/C mice [41]. In the same study it was found that BV/TV in the fifth lumbar vertebra increased between the ages of 2 and 12 months [41]. In contrast, Buie et al. [30] reported stable BV/TV in C57Bl/6 J mice in the third lumbar vertebra between the ages of 3 and 7 months, and Glatt et al. [42] found a decline in BV/TV in female C57Bl/6 J mice from 2 months old on in the fifth lumbar vertebra. In general, declines in the long bones have been observed from an early age on [41–44]. It thus seems that development of BV/TV is different in caudal vertebrae vs. the long bones.

When investigating bone dynamic parameters, it was found that both bone formation rate and bone resorption rate were elevated for OVX compared to SHM, with the bone resorption rate exceeding the bone formation rate in OVX, indicating high-turnover bone loss. Similarly, Bain et al. [36] found an increase in bone resorption determined from [^{3}H]tetracycline assay in the femur and thoracic vertebra but failed to show an increase in bone formation rate between OVX and SHM in the tibia 4 weeks after

ovariectomy. In our study, differences in BFR between OVX and SHM were also not present at this time point. Likewise, Kimble et al. [37] found an increase in bone resorption, as assessed by an increased osteoclast number per surface and percentage of bone covered by resorption surfaces in the tibia 2 weeks after ovariectomy. In contrast to our study, Okada et al. [45] reported increases in bone formation rate and bone resorption rate already at 2 weeks after ovariectomy as determined from biochemical markers in blood, with the bone resorption rate exceeding the bone formation rate, as determined from a decrease in BV/TV. Iwaniec et al. [18] did not find significant differences in BFR or osteoclast surface in either femur or lumbar vertebra between ovariectomy and sham groups. The differences in these findings might lie in the differences between skeletal sites and the sensitivity of the methods. An improvement in our analysis, compared to previous studies, is that bone formation and resorption parameters could be evaluated within the same bone at multiple time points, increasing statistical power. A further advantage is that the parameters are calculated in 3D and, thus, include more bone, through which the analysis picks up differences more readily.

Regarding the mechanical properties, we observed that the stiffness of the sixth caudal vertebra was significantly reduced in OVX compared to SHM. In agreement, several other investigators have reported similar reductions in mechanical properties after OVX [17, 46]. Interestingly, an additional observation of our study was that the load-carrying capacity of the trabecular bone reduced drastically, confirming the importance of cortical bone for mechanical stability.

There were several limitations associated with our study. The general disadvantages of a mouse model, including the lack of fragility fractures, the continuation of growth, and the speed of bone loss, also apply to our study. However, even though fragility fractures were not present, as in any rodent model of osteoporosis, the stiffness of the bone did reduce significantly. Furthermore, the speed of bone loss in the mouse is faster than that in rats or humans but is very predictable and similar for all mice (as they have the same genetic background), which is a requirement for a relevant model. Thus, in our eyes these disadvantages are surmounted by the advantages of the mouse model.

A limitation of our technique in the extraction of dynamic parameters is that only active sites of formation and resorption are captured, unlike in histology where the total amount of sites can be seen, with a distinction between active and nonactive sites. Furthermore, dynamic parameters were investigated at 2-week intervals. While this allowed investigation of changes in dynamic parameters over time within the same animal, intermediate changes within the 2-week time span could not be captured, leading to a reduction of the actual values for formation and resorption.

A drawback of the longitudinal setup in our study is the effect of radiation. Mice received a dose of 640 mGy per scan, leading to a total dose of 3.8 Gy (the scan at the last time point has no influence). This dose is higher than doses that have been reported previously to have no effect on the bone microstructure in C57Bl/6 mice [19, 30] or rats [47]. In a study where rats were scanned at nine time points, however, the dose was higher; but still no negative effect of radiation was found in the bone microstructure [48]. In a recent study it was found that two scans at 776 mGy per scan already influenced the bone microstructure negatively in 10-week-old male C57Bl/6 mice, while the effects were not significant at a dose of 434 mGy per scan. Nevertheless, in this study the right and left legs were compared, which have been reported to differ sometimes significantly even without a difference in treatment [30]. It is difficult to say what dose is still acceptable because this depends largely on the age of the mice (the younger, the more sensitive) and skeletal site (the more hematopoietic cells, the more sensitive). Therefore, the effect of radiation should always be considered in planning longitudinal studies. In a radiation control study performed before the start of this experiment, no detrimental effects of radiation were found on the bone microstructure or biochemical markers at a dose of 3 Gy (data not shown). Also, if the radiation would have had an effect, a decrease in bone mass for the sham mice would be anticipated, which did not occur.

In conclusion, we showed that ovariectomy led to (1) decreased bone mass, (2) high-turnover bone loss, and (3) reduced bone stiffness in the sixth caudal vertebra of C57Bl/6 J mice. The added value of our study was that dynamic parameters were calculated over time within single animals, allowing the monitoring of transient progression in remodeling rates, and included bone resorption rates. From our findings, we conclude that the sixth caudal vertebra of C57Bl/6 J mice is a suitable model for postmenopausal osteoporosis. Firstly, it shows similarities to the human progression of osteoporosis in static, dynamic, and mechanical parameters; and secondly, it is accessible for high-resolution imaging and nondestructive stiffness analysis.

Acknowledgements The authors gratefully acknowledge funding from the European Union for the Osteoporotic Virtual Physiological Human Project (FP7-ICT2008-223865), funding from the Whitaker Foundation, and computational time from the Swiss National Supercomputing Center (CSCS, Manno, Switzerland). We thank Peter Schwilch and Marco Hitz for technical assistance with the mouse holder and the statistical consulting team offered by the Seminar for Statistics at the ETH Zurich.

References

1. Ström O, Borgström F, Kanis JA, Compston J, Cooper C, McCloskey EV, Jönsson B (2011) Osteoporosis: burden, health care provision and opportunities in the EU. Arch Osteoporos. doi:10.1007/s11657-011-0060-1
2. Reinwald S, Burr D (2008) Review of nonprimate, large animal models for osteoporosis research. J Bone Miner Res 23:1353–1368
3. Kimmel DB (1996) Animal models for in vivo experimentation in osteoporosis research. In: Marcus R, Feldman D, Kelsey J (eds) Osteoporosis. Academic Press, San Diego, pp 671–690
4. Kalu DN (1991) The ovariectomized rat model of postmenopausal bone loss. Bone Miner 15:175–191
5. Brouwers JEM, Lambers FM, Gasser JA, van Rietbergen B, Huiskes R (2008) Bone degeneration and recovery after early and late bisphosphonate treatment of ovariectomized Wistar rats assessed by in vivo micro-computed tomography. Calcif Tissue Int 82:202–211
6. Boyd SK, Davison P, Müller R, Gasser JA (2006) Monitoring individual morphological changes over time in ovariectomized rats by in vivo micro-computed tomography. Bone 39:854–862
7. Waarsing JH, Day JS, van der Linden JC, Ederveen AG, Spanjers C, De Clerck N, Sasov A, Verhaar JA, Weinans H (2004) Detecting and tracking local changes in the tibiae of individual rats: a novel method to analyse longitudinal in vivo micro-CT data. Bone 34:163–169
8. Wronski TJ, Dann LM, Scott KS, Cintron M (1989) Long-term effects of ovariectomy and aging on the rat skeleton. Calcif Tissue Int 45:360–366
9. Tian XY, Liu XQ, Chen HY, Setterberg RB, Li M, Jee WS (2008) Greater efficacy of alfacalcidol in the red than in the yellow marrow skeletal sites in adult female rats. J Musculoskelet Neuronal Interact 8:257–266
10. Wronski TJ, Dann LM, Horner SL (1989) Time course of vertebral osteopenia in ovariectomized rats. Bone 10:295–301
11. Miyakoshi N, Sato K, Abe T, Tsuchida T, Tamura Y, Kudo T (1999) Histomorphometric evaluation of the effects of ovariectomy on bone turnover in rat caudal vertebrae. Calcif Tissue Int 64:318–324
12. Li M, Shen Y, Qi H, Wronski TJ (1996) Comparative study of skeletal response to estrogen depletion at red and yellow marrow sites in rats. Anat Rec 245:472–480
13. Klein RF (2008) Genetics of osteoporosis—utility of mouse models. J Musculoskelet Neuronal Interact 8:287–290
14. Alexander JM, Bab I, Fish S, Müller R, Uchiyama T, Gronowicz G, Nahounou M, Zhao Q, White DW, Chorev M, Gazit D, Rosenblatt M (2001) Human parathyroid hormone 1–34 reverses bone loss in ovariectomized mice. J Bone Miner Res 16:1665–1673
15. Cano A, Dapia S, Noguera I, Pineda B, Hermenegildo C, del Val R, Caeiro JR, Garcia-Perez MA (2008) Comparative effects of 17beta-estradiol, raloxifene and genistein on bone 3D microarchitecture and volumetric bone mineral density in the ovariectomized mice. Osteoporos Int 19:793–800
16. Bouxsein ML, Myers KS, Shultz KL, Donahue LR, Rosen CJ, Beamer WG (2005) Ovariectomy-induced bone loss varies among inbred strains of mice. J Bone Miner Res 20:1085–1092
17. Li CY, Schaffler MB, Wolde-Semait HT, Hernandez CJ, Jepsen KJ (2005) Genetic background influences cortical bone response to ovariectomy. J Bone Miner Res 20:2150–2158
18. Iwaniec UT, Yuan D, Power RA, Wronski TJ (2006) Strain-dependent variations in the response of cancellous bone to ovariectomy in mice. J Bone Miner Res 21:1068–1074
19. Klinck J, Boyd SK (2008) The magnitude and rate of bone loss in ovariectomized mice differs among inbred strains as determined by longitudinal in vivo micro-computed tomography. Calcif Tissue Int 83:70–79
20. Webster D, Wasserman E, Ehrbar M, Weber F, Bab I, Müller R (2010) Mechanical loading of mouse caudal vertebrae increases trabecular and cortical bone mass-dependence on dose and genotype. Biomech Model Mechanobiol 9:737–747
21. Lambers FM, Schulte FA, Kuhn G, Webster DJ, Muller R (2011) Mouse tail vertebrae adapt to cyclic mechanical loading by increasing bone formation rate and decreasing bone resorption rate as shown by time-lapsed in vivo imaging of dynamic bone morphometry. Bone. doi:10.1016/j.bone.2011.08.035
22. Reginster JY, Sarlet N, Lecart MP (2005) Fractures in osteoporosis: the challenge for the new millennium. Osteoporos Int 16(Suppl 1):S1–S3
23. Bilezikian JP, Matsumoto T, Bellido T, Khosla S, Martin J, Recker RR, Heaney R, Seeman E, Papapoulos S, Goldring SR (2009) Targeting bone remodeling for the treatment of osteoporosis: summary of the proceedings of an ASBMR workshop. J Bone Miner Res 24:373–385
24. Egermann M, Goldhahn J, Schneider E (2005) Animal models for fracture treatment in osteoporosis. Osteoporos Int 16(Suppl 2):S129–S138
25. Mosekilde L, Danielsen CC, Knudsen UB (1993) The effect of aging and ovariectomy on the vertebral bone mass and biomechanical properties of mature rats. Bone 14:1–6
26. Fonseca D, Ward WE (2004) Daidzein together with high calcium preserve bone mass and biomechanical strength at multiple sites in ovariectomized mice. Bone 35:489–497
27. Brouwers JEM, Lambers FM, van Rietbergen B, Ito K, Huiskes R (2009) Comparison of bone loss induced by ovariectomy and neurectomy in rats analyzed by in vivo micro-CT. J Orthop Res 27:1521–1527
28. Silva MJ, Brodt MD, Uthgenannt BA (2004) Morphological and mechanical properties of caudal vertebrae in the SAMP6 mouse model of senile osteoporosis. Bone 35:425–431
29. Schulte FA, Lambers FM, Kuhn G, Müller R (2011) In vivo micro-computed tomography allows direct three-dimensional quantification of both bone formation and bone resorption parameters using time-lapsed imaging. Bone 48:433–442
30. Buie HR, Moore CP, Boyd SK (2008) Postpubertal architectural developmental patterns differ between the L3 vertebra and proximal tibia in three inbred strains of mice. J Bone Miner Res 23:2048–2059
31. Bouxsein ML, Boyd SK, Christiansen BA, Guldberg RE, Jepsen KJ, Müller R (2010) Guidelines for assessment of bone microstructure in rodents using micro-computed tomography. J Bone Miner Res 25:1468–1486
32. Thevenaz P, Ruttimann UE, Unser M (1998) A pyramid approach to subpixel registration based on intensity. IEEE Trans Image Process 7:27–41
33. Webster DJ, Morley PL, van Lenthe GH, Müller R (2008) A novel in vivo mouse model for mechanically stimulated bone adaptation—a combined experimental and computational validation study. Comput Methods Biomech Biomed Eng 11:435–441
34. Christen P, van Rietbergen B, Lambers FM, Müller R, Ito K (2011) Bone morphology allows estimation of loading history in a murine model of bone adaptation. Biomech Model Mechanobiol. doi:10.1007/s10237-011-0327-x
35. Melton LJ 3rd, Christen D, Riggs BL, Achenbach SJ, Müller R, van Lenthe GH, Amin S, Atkinson EJ, Khosla S (2010) Assessing forearm fracture risk in postmenopausal women. Osteoporos Int 21:1161–1169
36. Bain SD, Bailey MC, Celino DL, Lantry MM, Edwards MW (1993) High-dose estrogen inhibits bone resorption and

stimulates bone formation in the ovariectomized mouse. J Bone Miner Res 8:435–442
37. Kimble RB, Bain S, Pacifici R (1997) The functional block of TNF but not of IL-6 prevents bone loss in ovariectomized mice. J Bone Miner Res 12:935–941
38. Parfitt AM (1994) Osteonal and hemi-osteonal remodeling: the spatial and temporal framework for signal traffic in adult human bone. J Cell Biochem 55:273–286
39. Vande Berg BC, Malghem J, Lecouvet FE, Maldague B (2001) Normal bone marrow: dynamic aspects in magnetic resonance imaging. J Radiol 82:127–135
40. Donnelly EH, Nemhauser JB, Smith JM, Kazzi ZN, Farfan EB, Chang AS, Naeem SF (2010) Acute radiation syndrome: assessment and management. South Med J 103:541–546
41. Willinghamm MD, Brodt MD, Lee KL, Stephens AL, Ye J, Silva MJ (2010) Age-related changes in bone structure and strength in female and male BALB/c mice. Calcif Tissue Int 86:470–483
42. Glatt V, Canalis E, Stadmeyer L, Bouxsein ML (2007) Age-related changes in trabecular architecture differ in female and male C57Bl/6 J mice. J Bone Miner Res 22:1197–1207
43. Halloran BP, Ferguson VL, Simske SJ, Burghardt A, Venton LL, Majumdar S (2002) Changes in bone structure and mass with advancing age in the male C57Bl/6 J mouse. J Bone Miner Res 17:1044–1050
44. Brodt MD, Silva MJ (2010) Aged mice have enhanced endocortical response and normal periosteal response compared with young-adult mice following 1 week of axial tibial compression. J Bone Miner Res 25:2006–2015
45. Okada Y, Morimoto I, Ura K, Nakano Y, Tanaka Y, Nishida S, Nakamura T, Eto S (1998) Short-term treatment of recombinant murine interleukin-4 rapidly inhibits bone formation in normal and ovariectomized mice. Bone 22:361–365
46. Ward WE, Fonseca D (2007) Soy isoflavones and fatty acids: effects on bone tissue postovariectomy in mice. Mol Nutr Food Res 51:824–831
47. Waarsing JH, Day JS, Verhaar JA, Ederveen AG, Weinans H (2006) Bone loss dynamics result in trabecular alignment in aging and ovariectomized rats. J Orthop Res 24:926–935
48. Brouwers JEM, van Rietbergen B, Huiskes R (2007) No effects of in vivo micro-CT radiation on structural parameters and bone marrow cells in proximal tibia of Wistar rats detected after eight weekly scans. J Orthop Res 25:1325–1332